

Optically-pumped dynamic nuclear hyperpolarization in ^{13}C enriched diamond

Anna J. Parker, Keunhong Jeong, Claudia E. Avalos, Birgit J. M. Hausmann,

Christophoros C. Vassiliou, Alexander Pines, and Jonathan P. King

*Department of Chemistry, University of California, Berkeley, California 94720, United States and
Materials Sciences Division, Lawrence Berkeley National Laboratory, Berkeley, California 94720, United States*

(Dated: November 26, 2021)

We investigate nuclear spin hyperpolarization from nitrogen vacancy centers in isotopically enriched diamonds with ^{13}C concentrations up to 100%. ^{13}C enrichment leads to hyperfine structure of the nitrogen vacancy electron spin resonance spectrum and as a result the spectrum of dynamic nuclear polarization. We show that strongly-coupled ^{13}C spins in the first shell surrounding a nitrogen vacancy center generate resolved hyperfine splittings, but do not act as an intermediary in the transfer of hyperpolarization of bulk nuclear spins. High levels of ^{13}C enrichment are desirable to increase the efficiency of hyperpolarization for magnetic resonance signal enhancement, imaging contrast agents, and as a platform for quantum sensing and many-body physics.

The last decade has witnessed rapid strides in the development of quantum technologies based on atom-like defect centers in solids^{1,2}, such as the negatively-charged nitrogen vacancy (NV^-) center³. The NV^- is a system of six localized electrons in diamond with a total spin of 1, whose properties have drawn attention from various scientific fields. For example, optical initialization of the NV^- spin state⁴, long electron spin coherence times exceeding 1 ms^{5,6}, and optical spin state readout⁷ have made the defect a model platform for quantum information processing⁸⁻¹⁰, simulation^{11,12} and metrology¹³⁻¹⁵.

Nearly all of these technologies require knowledge of and capitalization upon the interactions of the NV^- center with nearby nuclear spins both in and external to the diamond. Tuning the ^{13}C concentration by isotopic growth techniques¹⁶ enables a variety of quantum technology schemes. For instance, in the limit of low nuclear concentrations ($\leq 1\%$), NV^- - ^{13}C pairs can form quantum registers¹⁷⁻¹⁹ with increased sensing resolution^{20,21} and sensitivity²². At slightly higher concentrations ($\sim 10\%$), a single NV^- center can be coupled to a number of ^{13}C nuclei to form the node of a quantum information processor, allowing the indirect fast actuation and universal quantum control on the nuclear spins via the electronic qubit^{23,24}. At high concentrations beyond 50% and approaching 100% where internuclear couplings become significant, hybridized nuclear spin states enable decoherence protected subspaces²⁵ where classical information can be stored. This also forms a versatile system to study various condensed matter phenomena in the strongly dipolar coupled quantum networks²⁶, including notions of quantum transport²⁷, localization and criticality^{28,29}, and Floquet many-body phases³⁰⁻³².

Additionally, integrated NV^- -nuclear spin systems provide an exciting opportunity for long-standing Nuclear Magnetic Resonance (NMR) and Magnetic Resonance Imaging (MRI) technologies. While NMR and MRI are indispensable tools to the fields of chemistry, biology, engineering and medicine, their sensitivity relies on nuclear spin initialization (i.e. polarization), which at best reaches 10^{-4} at room temperature. In stark contrast to the weak magnetization of nuclear spins, opti-

cal pumping hyperpolarizes the NV^- spin state beyond thermal equilibrium at arbitrary temperature and over a wide range of magnetic fields³³. As a result, a number of schemes for creating nuclear spin hyperpolarization with NV^- centers based on traditional dynamic nuclear polarization (DNP) methods³⁴ have been reported in the recent literature³⁵⁻⁴³. These schemes propose the use of hyperpolarized ^{13}C nuclei in diamond for use as MRI contrast agents⁴⁴ as well as a platform for polarization transfer to external nuclei⁴³ for enhanced magnetic resonance signal from arbitrary samples. In these cases, the low natural abundance (1.1%) of ^{13}C nuclear spins limits the efficiency of hyperpolarization and it is desirable to work with ^{13}C enriched materials.

Here, we report NV^- DNP hyperpolarization of ^{13}C enriched diamonds. Our methods result in significant ^{13}C bulk polarizations approaching 0.1% at approximately 0.5 T in a variety of samples, an enhancement of three orders of magnitude over thermal polarization. We show how isotopic enrichment imparts a complex structure to the electron spin resonance spectrum and corresponding DNP spectrum. The DNP spectra lend insight to the mechanism of polarization transfer, illustrating that NV^- centers and the first shell of ^{13}C spins behave as a strongly coupled system that transfers polarization directly to weakly coupled nuclear spins. These findings open the path to their use as efficient external polarizing agents, and for applications in quantum technologies.

In this work we employ continuous-wave (CW) DNP to hyperpolarize ^{13}C nuclei in a set of single crystal diamonds at a magnetic field of approximately 472 mT with the NV^- crystal axis aligned along the magnetic field. A schematic of the DNP pulse sequence is given in Figure 1a. Each experiment begins with a set of 90° pulses to destroy any thermal ^{13}C polarization before a recovery time t_{rec} where ^{13}C polarization builds under continuous optical and microwave irradiation. The laser optically pumps the NV^- center to continually initialize its spin state, while microwave irradiation has the effect of transferring spin polarization between NV^- and ^{13}C spins, thus hyperpolarizing the ^{13}C spins and producing enhanced NMR signals. The hyperpolarized ^{13}C NMR spectra of

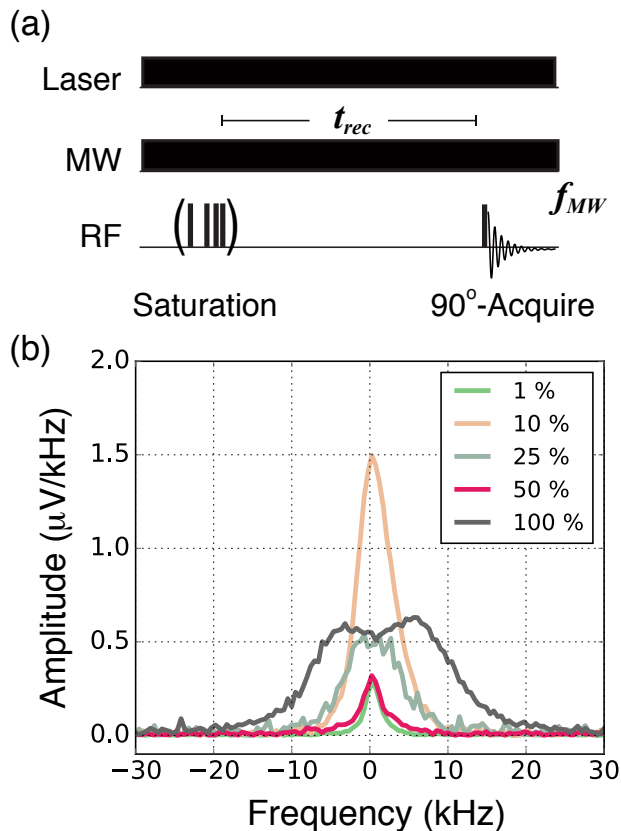


FIG. 1: CW-DNP with NV^- centers. A schematic for the CW-DNP experiment is shown in (a). The experiment begins with a series of 90° pulses to destroy ^{13}C polarization, after which the ^{13}C polarization builds under continuous optical and microwave excitation. The microwave frequency f_{MW} is swept to find the optimum frequency. After the ^{13}C nuclear polarization builds during a recovery time t_{rec} , a single 90° pulse is applied and the NMR signal is acquired. The spectra of the hyperpolarized ^{13}C NMR resulting from optimizing f_{MW} and the polarization buildup time are shown in (b) for samples with a natural abundance (1.1%) ^{13}C and 10, 25, 50, and 100% ^{13}C enrichment.

each sample are shown in Figure 1b, where the effects of the nuclear dipole-dipole couplings are apparent in the doublet spectrum of the 100% ^{13}C diamond.

In a field of 472 mT, NV^- spin transitions are observed at approximately 16.1 GHz and 10.3 GHz (Fig. 2a). In this work we focus on the higher-frequency transition. We read out the NV^- spin state via optically-detected magnetic resonance (ODMR), where the NV^- fluorescence intensity is monitored while sweeping the microwave frequency. Because the $m_s = \pm 1$ states are more likely to relax via intersystem crossing to the ground electronic state, resonant microwave excitation produces a detectable change in the NV^- fluorescence intensity³. ^{13}C spins within the first shell of nuclei, those directly

adjacent to the NV^- defect, are strongly coupled to the NV^- spin and give a resolved hyperfine structure (Fig. 2). In a ^{13}C enriched sample, the three nearest-neighbor sites are occupied by 0, 1, 2, or 3 ^{13}C nuclei with the balance occupied by spinless ^{12}C . The ODMR spectrum is therefore a superposition of 4 distinct patterns of hyperfine splittings with relative intensities determined by the degree of enrichment. The pattern of hyperfine splittings in Fig. 2 is consistent with the known ^{13}C - NV^- hyperfine tensor for first-shell nuclear spins⁴⁶.

The DNP process involves driving NV^- spin transitions to transfer polarization to nearby ^{13}C spins. The microscopic mechanism of DNP depends on the width of the electron spin spectrum relative to the nuclear Larmor frequency and also on interactions between the electron spins³⁴. In our experiments the solid effect, cross effect, and thermal mixing mechanisms of DNP all potentially contribute, and are difficult to distinguish. Regardless of the local DNP mechanism, nuclear spin diffusion transports polarization to bulk ^{13}C spins that do not interact directly with the NV^- center. In general, the DNP intensity has an antisymmetric frequency dependence and is related to the intensity of the ODMR spectrum (Fig. 3), consistent with DNP mechanisms where the EPR spectrum is broader than the nuclear Larmor frequency. Interestingly, this trend holds for the satellite peaks induced by the strongly hyperfine-coupled ^{13}C spins in the first shell, indicating that direct driving of the strongly-coupled hyperfine transition does not generate bulk polarization. This contrasts with NV^- hyperpolarization near a level anti-crossing where highly mixed electron-nuclear spin states result in hyperpolarization of first-shell ^{13}C which is then transported to bulk nuclear spins³⁶. Here, the symmetric intensities of the hyperfine-induced DNP satellites and the derivative DNP patterns at each satellite transition indicate the polarization of the first-shell ^{13}C spins does not play a role in the bulk DNP, other than to induce a splitting of the NV^- spectrum.

The level of maximum hyperpolarization is sample dependent due to the varied concentration of ^{13}C , NV^- centers, and other paramagnetic defects that cause nuclear spin relaxation, see Table I. The highest level of polarization was achieved in the natural abundance diamond, which has the highest NV^- concentration while the highest total magnetization occurred in the 100% diamond. The 100% ^{13}C diamond also exhibited the fastest buildup of hyperpolarization (Fig. 4), suggesting that the enhanced rate of nuclear spin diffusion more efficiently transports polarization to bulk nuclei. All other parameters being equal, we expect 100% ^{13}C diamonds to be optimum for MRI contrast and polarization transfer applications. We have shown that, despite the spectral complexity associated with multiple strong hyperfine couplings, hyperpolarization can be efficiently transferred to bulk nuclear spins. Furthermore, the control we demonstrate over bulk nuclear spin polarization in samples with a high nuclear spin concentration provide insight for and enable development of quantum technolo-

gies employing strongly-coupled spin systems.

Acknowledgement

This work was supported by the U.S. Department of Energy, Office of Science, Basic Energy Sciences under Contract No. DE-AC02-05CH11231. The authors thank Dr. Ashok Ajoy for helpful discussions and Dr. Melanie Drake and Prof. Jeffrey Reimer for providing the natural abundance sample. This study was made possible by the help of Joseph Tabeling at Applied Diamond Inc./Delaware Diamond Knives for the custom synthesis of the samples used in this study.

I. MATERIALS AND METHODS

^{13}C enriched diamonds were grown by chemical vapor deposition (Applied Diamond Inc.) using ^{13}C enrichments of methane with 600 ppm nitrogen as a precursor. ^{13}C concentrations of 10%, 25%, 50%, and 100% ^{13}C were used. These samples were compared to a sample grown by high-pressure high-temperature (HPHT) diamond synthesis (Sumitomo Electric Carbide, Inc.) with a substitutional nitrogen concentration of approximately 200 ppm and ^{13}C concentration of 1.1% (natural abundance). All samples were irradiated with 1 MeV electrons at a fluence of 10^{18} cm^{-2} (Prism Gem LLC) and annealed at 800°C for 2 h to produce an NV^- concentration of 1-10 ppm. Optically detected magnetic resonance (ODMR) and DNP were performed in a purpose-built instrument consisting of a custom probe fixed in an electromagnet (GMW Associates, Model 3472-50 with Danfysik 858 power supply). The probe includes a radiofrequency circuit for inductive NMR excitation and detection, a goniometer for two-axis alignment of the defect axis along the magnetic field, a 3 mm wire loop for microwave excitation (Agilent E8257D signal generator), and optical access to the sample (532 nm Coherent Verdi G5 laser). For all DNP experiments, the amplitude of the microwave frequency was set to 10 dBm and amplified with 3 W amplifier (Mini-Circuits ZVE-3W-183+) before being sent to the 3 mm loop. The NMR circuit includes a 30-turn planar coil of 46 AWG copper wire, with capacitance added to impedance-match the circuit at 5.06 MHz. The NMR component of DNP experiments are carried out with a Magritek Kea² console. For ODMR measurements, the microwave amplitude was modulated 100% at 200 Hz from the reference signal of the lock-in amplifier (Stanford Research Systems, SR830) and the fluorescence signal was detected with an avalanche photodiode (APD 410A, Thorlabs). The lock-in amplifier measured the in-phase component of the fluorescence signal at the modulation frequency using a time constant of 30 ms. A spectrum was acquired by stepping through a range of microwave frequency centered on the NV^- ESR,

where each step consists of changing the microwave frequency by one step, waiting 50 ms, and measuring the ODMR signal from the lock-in. These spectra were used to characterize the samples, align the defect axis along the magnetic field, and set the strength of the magnetic field as measured by the ensemble of NV^- defects for DNP experiments.

DNP experiments were carried out at 472.2 mT. A schematic of the DNP experiment is shown in Figure 1. A 532 nm laser with a beam diameter of approximately 5 mm is set to an output power of 1 W/cm^2 and applied continuously throughout experiments. The laser beam is kept large to irradiate the full surface of the diamond. A set of 90° pulses are used to destroy thermal ^{13}C polarization before waiting a time t_{rec} for ^{13}C polarization to build as a result of DNP processes. The microwave frequency is set to f_{MW} and applied continuously for the duration of t_{rec} . A simple 90 pulse-acquire experiment is then used to determine the ^{13}C NMR signal. This is repeated for a range of f_{MW} centered on the NV^- ESR to acquire the DNP spectrum of ^{13}C NMR signal as a function of microwave frequency f_{MW} . The ^{13}C NMR signal was compared by fitting the free induction decay (FID) at $f_{MW,i}$ to the FID of the signal with maximum enhancement by a scaling factor. All data are reported with error bars giving 95% confidence intervals for the scaling factors, taken from the standard deviation of the parameter estimates of the fit. All NMR raw data were acquired with Prospa (software supplied with the Kea² spectrometer) and exported for processing in Python with Matplotlib⁴⁷, SciPy and NumPy^{48,49} packages. Additional details on methods and data analysis can be found in the Supplemental Information.

Photoluminescence (PL) experiments in the Supplemental Information document were carried out with a homebuilt confocal microscope to gain a qualitative understanding of the defect content in each of the samples. The confocal microscope involves a 532 nm laser (Opto Engine LLC, MGL-III-532-200mW) directed to the sample through a microscope objective with $\text{NA} = 0.4$ (Nikon M Plan 20 ELWD). From this NA we estimate an excitation volume of $1.9 \times 10^5 \mu\text{m}^3$. The objective is also used to collect the fluorescence and direct it through a dichroic mirror to a spectrometer (Mightex HRS-BD1-025). The emission of the samples were collected using an approximate optical excitation power of 2.5 kW/cm^2 . We use the minimum optical power required to detect the emission spectra with the Mightex Spectrometer in order to suppress any changes in the emission spectra due to charge-state conversion between NV^- and NV^0 . Emission spectra were collected from sixteen random points in each of the samples. Each spectrum was averaged 256 times with an exposure time of 100 ms. The raw data were acquired using the software provided by Mightex for interfacing with the spectrometer, and exported for processing in Python.

Sample	D1	D2	D3	D4	D5
[^{13}C] (%)	1	10	25	50	100
T_{DNP} (s)	22.34 ± 0.06	59.55 ± 0.03	36.14 ± 0.02	42.94 ± 0.04	15.28 ± 0.02
Enhancement	$1264 \in [854, 2430]$	1094 ± 202	318 ± 22	138 ± 4	604 ± 11
P_{enh} (%)	$0.10 \in [0.071, 0.20]$	0.091 ± 0.017	0.026 ± 0.002	0.011 ± 0.0004	0.050 ± 0.0009

TABLE I: Summary of the polarization buildup time T_{DNP} , enhanced ^{13}C nuclear polarization (P_{enh}) and maximum DNP enhancement for each diamond sample.

-
- ¹ W. F. Koehl, B. B. Buckley, F. J. Heremans, G. Calusine, and D. D. Awschalom, *Nature* **479**, 84 (2011).
- ² M. Widmann, S.-Y. Lee, T. Rendler, N. T. Son, H. Fedder, S. Paik, L.-P. Yang, N. Zhao, S. Yang, I. Booker, et al., *Nature Materials* **14**, 164 (2015).
- ³ M. W. Doherty, N. B. Manson, P. Delaney, F. Jelezko, J. Wrachtrup, and L. C. L. Hollenberg, *Physics Reports* **528**, 1 (2013), ISSN 03701573, arXiv:1302.3288v1, URL <http://dx.doi.org/10.1016/j.physrep.2013.02.001>.
- ⁴ N. Manson and R. McMurtrie, *Journal of Luminescence* **127**, 98 (2007), proceedings of the Ninth International Meeting on Hole Burning, Single Molecule, and Related Spectroscopies: Science and Applications, Hole Burning, Single Molecule, and Related Spectroscopies: Science and Applications, URL <http://www.sciencedirect.com/science/article/B6TJH-4N56BY8-4/2/fe207946349634f71860c2b4ad4ebf3a>.
- ⁵ G. Balasubramanian, P. Neumann, D. Twitchen, M. Markham, R. Kolesov, N. Mizuochi, J. Isoya, J. Achard, J. Beck, J. Tissler, et al., *Nat Mater* **8**, 383 (2009).
- ⁶ D. J. Christle, A. L. Falk, P. Andrich, P. V. Klimov, J. U. Hassan, N. T. Son, E. Janzén, T. Ohshima, and D. D. Awschalom, *Nature Materials* **14** (2015).
- ⁷ M. W. Doherty, N. B. Manson, P. Delaney, and L. C. L. Hollenberg, *New Journal of Physics* **13**, 025019 (2011), URL <http://stacks.iop.org/1367-2630/13/i=2/a=025019>.
- ⁸ N. Yao, L. Jiang, A. Gorshkov, P. Maurer, G. Giedke, J. Cirac, and M. Lukin, *Nat Commun* **3**, 800 (2012), URL <http://dx.doi.org/10.1038/ncomms1788>.
- ⁹ B. Hensen, H. Bernien, A. E. Dréau, A. Reiserer, N. Kalb, M. S. Blok, J. Ruitenber, R. F. Vermeulen, R. N. Schouten, C. Abellán, et al., *Nature* **526**, 682 (2015).
- ¹⁰ P. V. Klimov, A. L. Falk, D. J. Christle, V. V. Dobrovitski, and D. D. Awschalom, *Science advances* **1**, e1501015 (2015).
- ¹¹ J. Cai, A. Retzker, F. Jelezko, and M. B. Plenio, *Nature Physics* **9**, 168 (2013).
- ¹² A. Ajoy and P. Cappellaro, *Phys. Rev. Lett.* **110**, 220503 (2013), URL <http://link.aps.org/doi/10.1103/PhysRevLett.110.220503>.
- ¹³ J. M. Taylor, P. Cappellaro, L. Childress, L. Jiang, D. Budker, P. R. Hemmer, A. Yacoby, R. Walsworth, and M. D. Lukin, *Nature Phys.* **4**, 810 (2008).
- ¹⁴ J. R. Maze, P. L. Stanwix, J. S. Hodges, S. Hong, J. M. Taylor, P. Cappellaro, L. Jiang, A. Zibrov, A. Yacoby, R. Walsworth, et al., *Nature* **455**, 644 (2008).
- ¹⁵ G. Balasubramanian, I.-Y. Chan, R. Kolesov, M. Al-Hmoud, C. Shin, C. Kim, A. Wojcik, P. R. Hemmer, A. Krüger, F. Jelezko, et al., *Nature* **445**, 648 (2008).
- ¹⁶ N. Bar-Gill, L. Pham, C. Belthangady, D. Le Sage, P. Cappellaro, J. Maze, M. Lukin, A. Yacoby, and R. Walsworth, *Nat. Commun.* **3**, 858 (2012), URL <http://dx.doi.org/10.1038/ncomms1856>.
- ¹⁷ M. V. G. Dutt, L. Childress, L. Jiang, E. Togan, J. Maze, F. Jelezko, A. S. Zibrov, P. R. Hemmer, and M. D. Lukin, *Science* **316**, 1312 (2007).
- ¹⁸ P. Neumann, R. Kolesov, B. Naydenov, J. Beck, F. Rempp, M. Steiner, V. Jacques, G. Balasubramanian, M. L. Markham, D. J. Twitchen, et al., *Nat Phys* **6**, 249 (2010).
- ¹⁹ A. Reiserer, N. Kalb, M. S. Blok, K. J. van Bemmel, T. H. Taminiau, R. Hanson, D. J. Twitchen, and M. Markham, *Physical Review X* **6**, 021040 (2016).
- ²⁰ A. Laraoui, F. Dolde, C. Burk, F. Reinhard, J. Wrachtrup, and C. A. Meriles, *Nature communications* **4**, 1651 (2013).
- ²¹ T. Rosskopf, J. Zopes, J. Boss, and C. Degen, arXiv preprint arXiv:1610.03253 (2016).
- ²² A. Ajoy, Y. Liu, and P. Cappellaro, arXiv preprint arXiv:1611.04691 (2016).
- ²³ N. Khaneja, *Phys. Rev. A* **76**, 032326 (2007).
- ²⁴ T. W. Borneman, C. E. Granade, and D. G. Cory, *Phys. Rev. Lett.* **108**, 140502 (2012), URL <http://link.aps.org/doi/10.1103/PhysRevLett.108.140502>.
- ²⁵ N. Kalb, A. A. Reiserer, P. C. Humphreys, J. J. Bakermans, S. J. Kamerling, N. H. Nickerson, S. C. Benjamin, D. J. Twitchen, M. Markham, and R. Hanson, *Science* **356**, 928 (2017).
- ²⁶ H. Weimer, N. Y. Yao, and M. D. Lukin, *Physical review letters* **110**, 067601 (2013).
- ²⁷ A. Ajoy and P. Cappellaro, *Phys. Rev. B* **87**, 064303 (2013), URL <http://link.aps.org/doi/10.1103/PhysRevB.87.064303>.
- ²⁸ N. Y. Yao, C. R. Laumann, S. Gopalakrishnan, M. Knap, M. Mueller, E. A. Demler, and M. D. Lukin, *Physical review letters* **113**, 243002 (2014).
- ²⁹ R. Nandkishore and D. A. Huse, *Annu. Rev. Condens. Matter Phys.* **6**, 15 (2015).
- ³⁰ V. Khemani, A. Lazarides, R. Moessner, and S. L. Sondhi, *Physical review letters* **116**, 250401 (2016).
- ³¹ D. V. Else and C. Nayak, *Physical Review B* **93**, 201103 (2016).
- ³² S. Choi, J. Choi, R. Landig, G. Kucsko, H. Zhou, J. Isoya, F. Jelezko, S. Onoda, H. Sumiya, V. Khemani, et al., *Nature* **543**, 221 (2017).
- ³³ E. Scott, M. Drake, and J. A. Reimer, *Journal of Magnetic Resonance* **264**, 154 (2016).
- ³⁴ T. Wenckebach, *Essentials of Dynamic Nuclear Polarization* (Spindrift, Burgh-Haamstede, The Netherlands, 2016), ISBN 978907.
- ³⁵ R. Fischer, A. Jarmola, P. Kehayias, and D. Budker, *Phys-*

- ical Review B - Condensed Matter and Materials Physics **87**, 1 (2013), ISSN 10980121, 1202.1072.
- ³⁶ G. A. Álvarez, C. O. Bretschneider, R. Fischer, P. London, H. Kanda, S. Onoda, J. Isoya, D. Gershoni, and L. Frydman, *Nature Communications* **6**, 8456 (2015), ISSN 2041-1723, 1412.8635, URL <http://www.nature.com/doi/10.1038/ncomms9456>.
- ³⁷ J. P. King, P. J. Coles, and J. A. Reimer, *Physical Review B - Condensed Matter and Materials Physics* **81**, 1 (2010), ISSN 10980121.
- ³⁸ J. Scheuer, I. Schwartz, Q. Chen, D. Schulze-Sunninghausen, P. Carl, P. Hofer, A. Retzker, H. Sumiya, J. Isoya, B. Luy, et al., *New Journal of Physics* **18**, 13040 (2016), ISSN 13672630, 1601.05967.
- ³⁹ D. E. J. Waddington, M. Sarracanie, H. Zhang, N. Salameh, D. R. Glenn, E. Rej, T. Gaebel, T. Boele, R. L. Walsworth, D. J. Reilly, et al., *Nature Communications* **8**, 1 (2016), ISSN 2041-1723, 1611.05167, URL <http://arxiv.org/abs/1611.05167>.
- ⁴⁰ E. Rej, T. Gaebel, D. E. J. Waddington, and D. J. Reilly, *arXiv* **1606.06822**, 1 (2016), ISSN 0002-7863, 1606.06822.
- ⁴¹ Q. Chen, I. Schwarz, F. Jelezko, A. Retzker, and M. B. Plenio, *Physical Review B - Condensed Matter and Materials Physics* **92**, 20 (2015), ISSN 1550235X, 1504.02368.
- ⁴² Q. Chen, I. Schwarz, F. Jelezko, A. Retzker, and M. B. Plenio, *Physical Review B - Condensed Matter and Materials Physics* **93**, 1 (2016), ISSN 1550235X, 1510.03256.
- ⁴³ J. P. King, K. Jeong, C. C. Vassiliou, C. S. Shin, R. H. Page, C. E. Avalos, H.-j. Wang, and A. Pines, *Nature Communications* **6**, 8965 (2015), ISSN 2041-1723, 1501.2897, URL <http://dx.doi.org/10.1038/ncomms9965>.
- ⁴⁴ E. Rej, T. Gaebel, T. Boele, D. E. J. Waddington, and D. J. Reilly, *Nature Communications* **6**, 8459 (2015), ISSN 2041-1723, arXiv:1502.06214v1, URL <http://dx.doi.org/10.1038/ncomms9459>.
- ⁴⁵ A. J. Parker, H.-J. Wang, Y. Li, A. Pines, and J. P. King, *Decoherence-protected transitions of nitrogen vacancy centers in 99% ¹³C-enriched diamond* (2015), arXiv:1506.05484.
- ⁴⁶ J. H. Shim, B. Nowak, I. Niemeyer, J. Zhang, F. D. Brandão, and D. Suter, arXiv:1307.0257 (2013).
- ⁴⁷ J. D. Hunter, *Computing In Science & Engineering* **9**, 90 (2007).
- ⁴⁸ S. van der Walt, S. C. Colbert, and G. Varoquaux, *Computing in Science & Engineering* **13**, 22 (2011).
- ⁴⁹ E. Jones, T. Oliphant, P. Peterson, et al., *SciPy: Open source scientific tools for Python* (2001-), URL "<http://www.scipy.org/>".
- ⁵⁰ T. Kennedy, J. Colton, J. Butler, R. Linares, and P. Doring, *Applied Physics Letters* **83**, 4190 (2003).
- ⁵¹ N. Boden and M. Mortimer, *Chemical Physics Letters* **21**, 538 (1973).
- ⁵² W. Li, R. Scheidegger, Y. Wu, A. Vu, and P. V. Prasad, *Journal of Magnetic Resonance Imaging* **27**, 678 (2008).

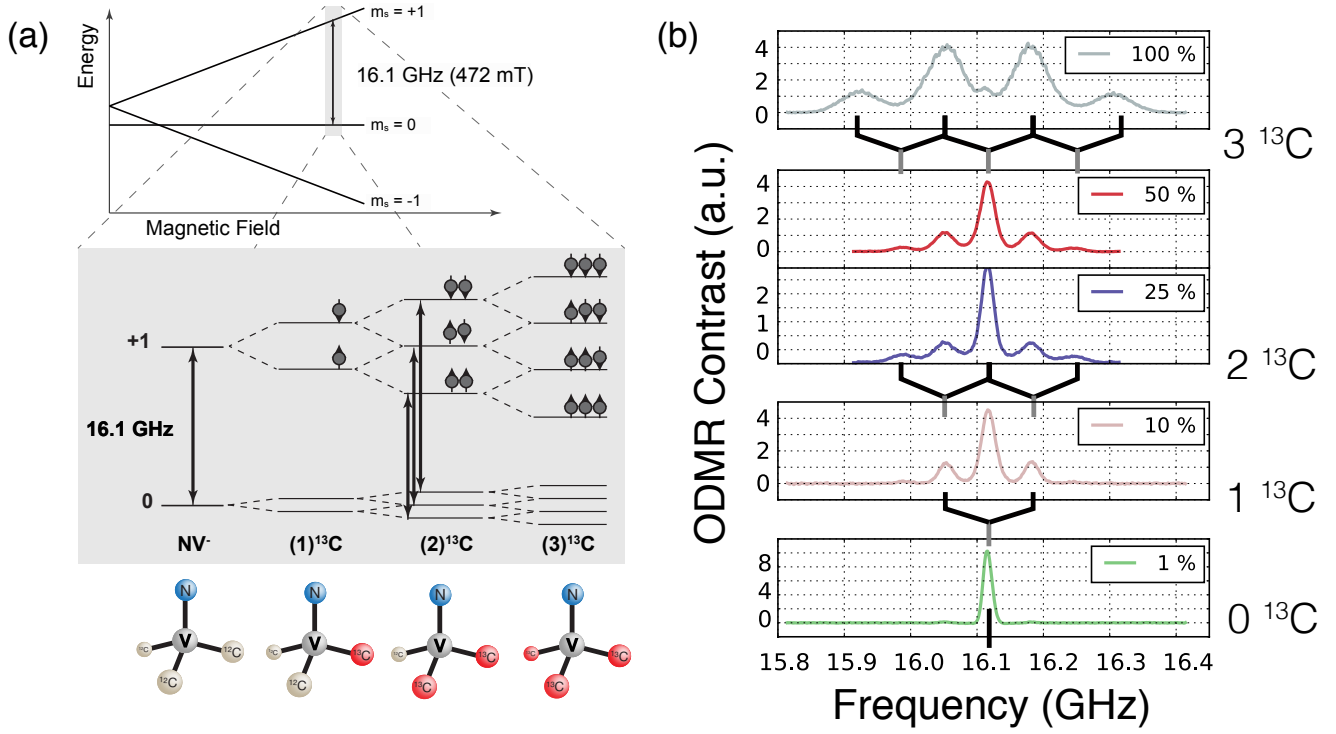


FIG. 2: The effect of ¹³C enrichment on the energy level structure and ODMR spectroscopy of NV⁻ centers. The energy level structure of the NV⁻ as a function of magnetic field strength is shown in (a), where the magnetic field regime relevant to DNP experiments is highlighted and expanded. In this work, we focus on the high energy transition from the NV⁻ $m_s = 0$ to $m_s = +1$ at 472 mT, which has a frequency of approximately 16.1 GHz. The strongest hyperfine interactions occur between the NV⁻ and its first-shell ¹³C nuclei, those directly adjacent to it. Occupation of the first-shell sites leads to a splitting in not only the NV⁻ $m_s = \pm 1$ levels, but also the $m_s = 0$ due to the anisotropic component of the coupling. The magnified energy level diagram shows how the NV⁻ spin states split into hyperfine states determined by the different possible combinations of nuclear spin, as 1, 2, and 3 carbons are added. Diagrams of the NV⁻ as well as the occupation of the first shell sites with ¹³C nuclei are given below the energy level diagram. The branching in these energy levels corresponds directly to the structure seen in the ODMR spectra of diamonds with varying ¹³C enrichment (b). A single line is observed for the $m_s = 0$ to $m_s = +1$ transition in NV⁻ spin state for a sample with a natural abundance (1.1%) of ¹³C, whereas a sample with 100% ¹³C enrichment exhibits a quartet for the same transition.⁴⁵

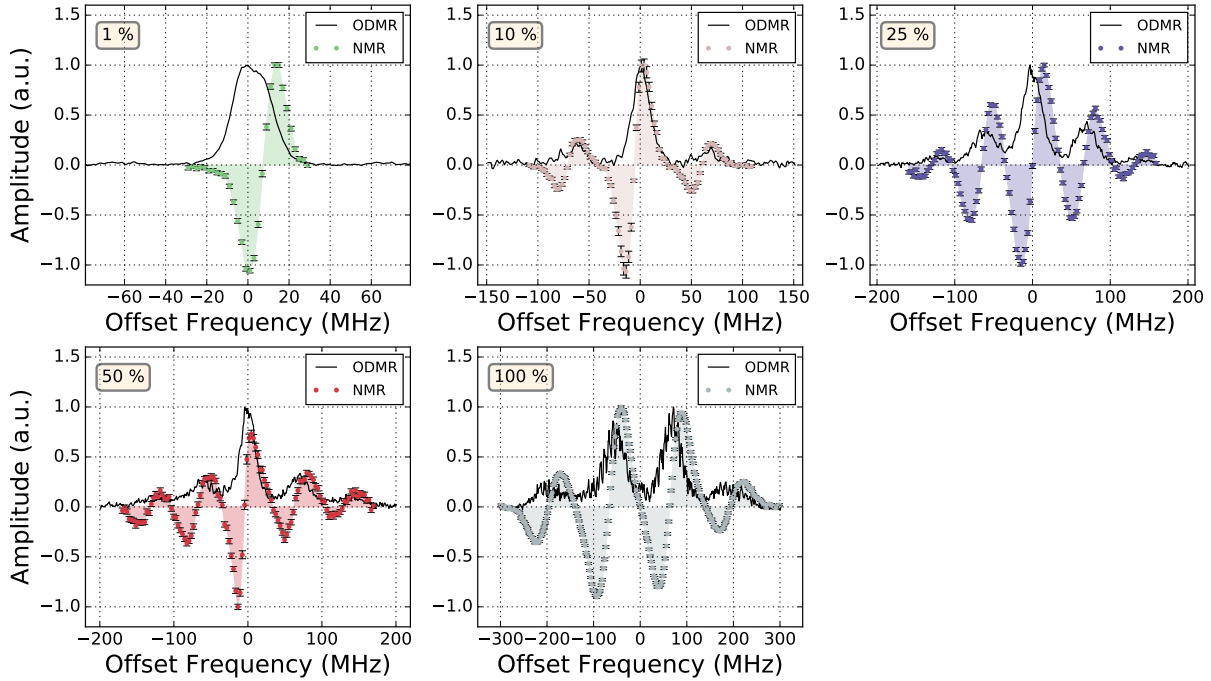


FIG. 3: DNP spectra of the various diamond samples. Normalized hyperpolarized ^{13}C NMR signal as a function of offset microwave frequency for each sample. The normalized ODMR data for each sample is given to show the corresponding high frequency transition of the NV^- ESR spectrum. CW-DNP experiments are performed at 472.1 - 473.0 mT, thus the microwave frequency is centered at approximately 16.1 GHz for the various samples with an ^{13}C NMR frequency of approximately 5.06 MHz. It should be noted the SNR of the ODMR spectra shown here differs from that of the ODMR spectra in Figure 2 because the two were acquired at different microwave amplitudes. The optimum microwave amplitude for DNP measurements is higher than the microwave amplitude for optimized ODMR contrast (see Materials and Methods).

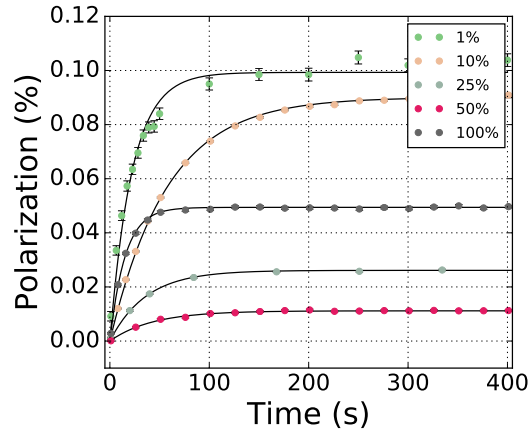


FIG. 4: ^{13}C polarization buildup curves are summarized for all samples involved in the study. Characteristic polarization buildup times T_{DNP} are given in Table I. The sample with 100% ^{13}C enrichment gives the fastest buildup and the largest signal. The maximum polarization as well as the second-fastest buildup rate is observed from the sample with a natural abundance of ^{13}C , which is likely due to it having the highest concentration of NV^- centers (see Supplemental Information).

II. SUPPLEMENTAL INFORMATION

In this document we summarize all data supporting the analysis of results and conclusions drawn in the body of the manuscript. All confidence intervals reported in this work correspond to 95% bounds.

A. Sample characterization

The samples acquired for this study include one with a natural abundance of ^{13}C grown by high-pressure high-temperature (HPHT) methods (D1) in addition to four samples grown by chemical vapor deposition (CVD, Applied Diamond Inc.). The CVD samples (D2-D5) were grown with with added nitrogen precursor and varying levels of ^{13}C enriched methane to accomplish a distribution of ^{13}C concentrations. Sample parameters are summarized in Table SII. The photoluminescence (PL) spectrum of each sample (Fig. S5) was acquired in order to order to gain a qualitative understanding of the sample composition. The details on how the PL spectra were acquired are given in the Materials and Methods section. The PL spectrum of a diamond containing a high concentration of NV^- centers typically has four prominent features within the range of 560 - 750 nm. The two sharp peaks found roughly at 575 and 638 nm correspond to the zero phonon lines of the neutral (NV^0) and negatively-charged NV^- , respectively. The broad features red-shifted from each ZPL are the phonon side bands corresponding to higher vibrational levels of the excited states of each defect.

Most importantly, the PL spectra qualitatively demonstrate a large variation in the concentration of NV^- , NV^0 , and substitutional nitrogen (N_S , also called P1 centers) among even the CVD samples, preventing quantitative analysis of the polarization buildup rates. Also of note from the PL spectra is that sample D1 has a much larger ratio of $\text{NV}^-:\text{NV}^0$ than any of the CVD-grown samples. This is consistent with previous studies⁵⁰ and is attributed to higher levels of N_S , typical of HPHT growth, which act as donors to the NV^0 to achieve larger conversion to NV^- . These data indicate a higher NV^- concentration in sample D1, which provides an explanation for why the polarization buildup rate of sample D1 exceeds most of the buildup rates of the ^{13}C -enriched samples despite slow spin diffusion. Polarization buildup (T_{DNP}) and ^{13}C nuclear spin-lattice relaxation times ($T_{1,^{13}\text{C}}$) are summarized in Table SII.

B. Calibration of the ^{13}C nuclear polarization enhancement in diamond.

The long nuclear spin lattice relaxation times of ^{13}C in diamond as well as the low sensitivity of ^{13}C NMR at 5 MHz make detecting a thermal ^{13}C NMR signal challenging. We overcome this challenge by using a solid

echo pulse sequence⁵¹ (shown schematically in Figure 6) which extends the duration of the free induction decay via a spin-locking effect. The pulse sequence is originally carried out on the hyperpolarized ^{13}C NMR signal, which is fit with a biexponential function. We assume the thermally polarized signal has the same functional form, and we seek the scaling factor that relates the thermal and hyperpolarized signals. The schematic in Figure 6 shows detection of the hyperpolarized signal, which includes laser and microwave excitation at the optimized frequency. For measurement of the thermal signal, the same pulse sequence is used with the laser off, and the microwave frequency set to 13 GHz (far off resonance from any transition contributing to DNP).

For solid echo pulse measurements to be successful, the NMR 90 pulse length should be short relative to the evolution of the spins and τ should be short as possible relative to the decay of the FID to efficiently spin-lock the nuclear polarization in the transverse plane, otherwise coherence is lost rapidly and the spin-locking effect is diminished. In our experiment, 90 pulse lengths were in the range 1.0 - 2.5 μs . Typical parameters for an echo sequence with these samples involved acquiring the free-induction decay with 32 points at a dwell time of 0.5 μs and τ of 40 μs for 500 echoes. For the hyperpolarized signal, the polarization was allowed to build for a time of $4T_{DNP}$ (see Table SII).

The solid echo pulse sequence results in a time domain decay extended well beyond T_2^* of a true FID. We process the solid echo data with a moving average to smooth short timescale noise unrelated to the spin dynamics. The size of the window of the moving average varies based on the dynamics of the spin system, but ranges from 0.1 - 0.5 ms. Figure 7 demonstrates this processing.

Solid echo data for hyperpolarized and thermal signals of each sample is given in Figure 10. The 95% confidence interval of each biexponential model fit from the real component of the hyperpolarized data is underlaid in the figure. The thermal data are fit to this model with a scaling factor to estimate the amplitude of the thermal signal. Bootstrapping is used in order to gain proper estimates of the mean and variance of the amplitude of the thermal signal fitted from the hyperpolarized model data. Bootstrapping is carried out by saving thermal data sets in sets of 4 averages. Some thermal measurements require 1000-2000 datasets of 4 averages. These are randomly resampled with replacement approximately 10^4 times, where upon each resampling the data are averaged and a mean amplitude is fit. This produces a distribution of 10^4 fitted amplitudes whose mean and variance give a proper measure of the amplitude of the thermal ^{13}C NMR signal. The number of times to resample was chosen such that the values given for mean and variance are reproduced, despite using random resampling. Because acquiring thermal signal in some cases involves thousands of averages, the solid echo pulse sequences for these experiments are run with a recovery

Sample	D1	D2	D3	D4	D5
[^{13}C] (%)	1	10	25	50	100
Mass (mg)	4.4	12.4	10.6	5.9	9.3
T_{DNP} (s)	22.34 ± 0.06	59.55 ± 0.03	36.14 ± 0.02	42.94 ± 0.04	15.28 ± 0.02
$T_{1,^{13}\text{C}}$ (s)	13.08 ± 1.11	76.85 ± 3.70	51.18 ± 0.42	16.68 ± 2.20	10.33 ± 0.14
Enhancement	$1264 \in [854, 2430]$	1094 ± 202	318 ± 22	138 ± 4	604 ± 11
P_{enh} (%)	$0.10 \in [0.071, 0.20]$	0.091 ± 0.017	0.026 ± 0.002	0.011 ± 0.0004	0.050 ± 0.0009

TABLE II: Summary of parameters and maximum DNP enhancement for diamond samples. Values for T_{DNP} , $T_{1,^{13}\text{C}}$, the enhancement from DNP processes, and the enhanced ^{13}C nuclear polarization (P_{enh}) are measured at 470 mT.

time t_{rec} of approximately $T_{1,^{13}\text{C}}$ for efficiency. The amplitudes are then corrected with measured $T_{1,^{13}\text{C}}$ data to obtain the true amplitude of the thermal signal. These correction factors are given in the subcaptions of Figure 10.

It is clear from the D1 solid echo data in Figure 10(a) the thermal ^{13}C NMR signal is still dominated by noise. This measurement at least allows an assignment of a mean enhancement with upper and lower bounds to 95% confidence. While the errors in the amplitude of the thermal relative to the hyperpolarized ^{13}C NMR signal for D1 are normally distributed, the distribution of noise in the enhancement is not, so we cannot state a confidence interval in terms of 2σ . We instead find the bounds on the estimated relative amplitude of the thermal signal and convert these to bounds in enhancement. In the case of the ^{13}C -enriched samples, ^{13}C NMR signal is detected and therefore the errors in enhancement are normally

distributed. For these samples, we fit the mean enhancement by bootstrapping the thermal data and fitting to the hyperpolarized model data, and the variance of this enhancement gives us the confidence interval. Estimated values for relative amplitude of thermal ^{13}C NMR signals, final polarization in the hyperpolarized signal, as well as enhancements are given in Table SII.

With the exception of the sample with 25% ^{13}C enrichment, the nuclear T_1 measurements are carried out with a small-flip angle pulse sequence, described schematically in Figure 9. The angle of the small-flip pulse is calibrated from a nutation curve and the final T_1 value measured is corrected for the contribution of the small-flip pulse to relaxation⁵². We use small-flip angle pulse lengths of 0.5 - 1.5 μs with a typical spacing τ of 1 s. For each T_1 measurement the polarization is allowed to build for approximately $2T_{DNP}$. All $T_{1,^{13}\text{C}}$ measurements are given in Figure 8.

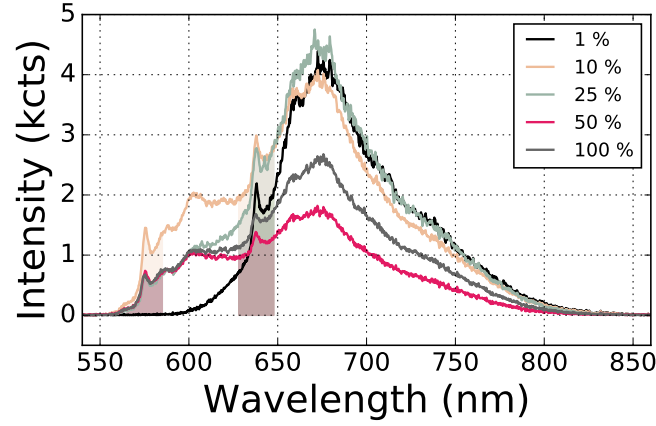


FIG. 5: Photoluminescence data. The trace for the emission from D1 (1% ^{13}C) is given in black to emphasize the difference in emission between HPHT-grown and CVD-grown samples. The majority of NV centers in sample D1 are negatively-charged. The NV^0 and NV^- ZPLs are highlighted.

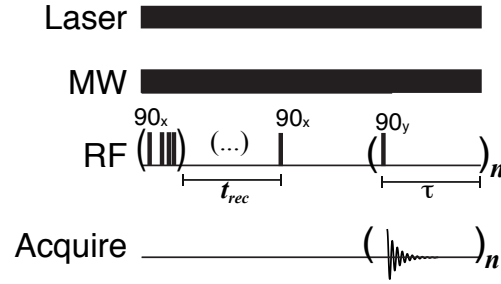


FIG. 6: Schematic of the solid echo pulse sequence for detecting hyperpolarized ^{13}C NMR at 5 MHz. The laser and microwave excitation are applied continuously, where the microwave frequency is set to the optimum frequency for DNP. The sequence begins with a series of 90° saturation pulses to ensure zero initial ^{13}C polarization. Polarization builds up for a time of t_{rec} . The solid echo sequence is initiated with a 90° pulse along the x axis, a delay of time τ called the “echo time”, following by a train of n 90° pulses along the y axis separated by τ . A free-induction decay is acquired after every 90_y° pulse. The 90_y° pulses follow a phase cycle of $[180, 0, 0, 180]$.

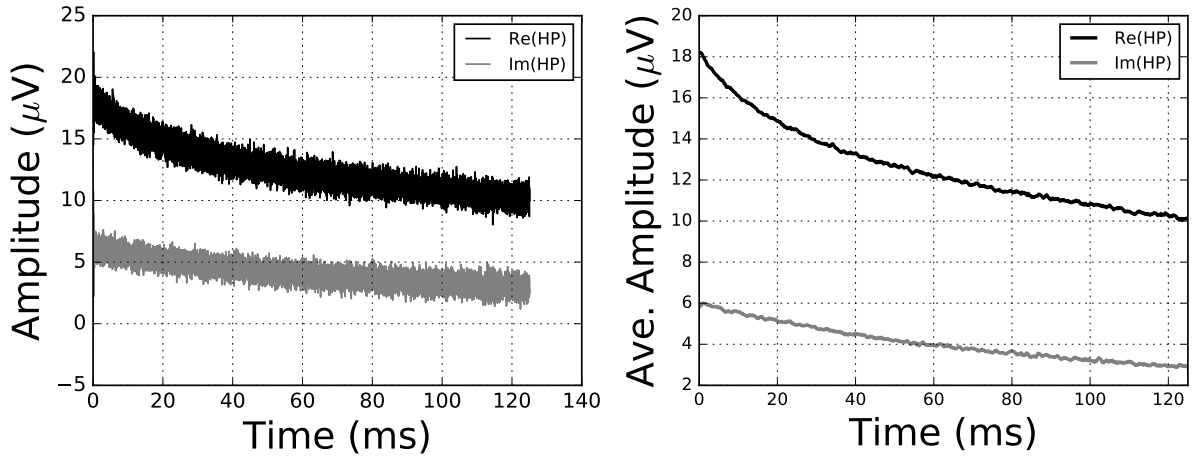
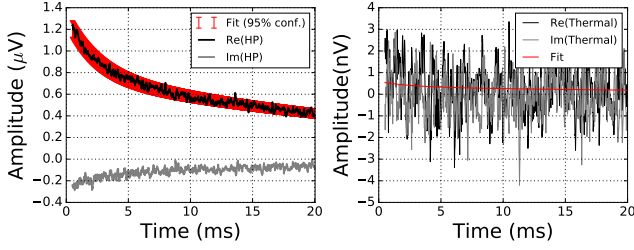
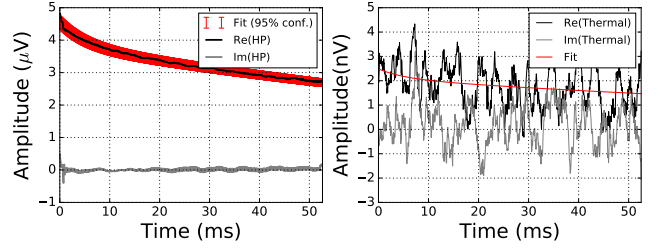


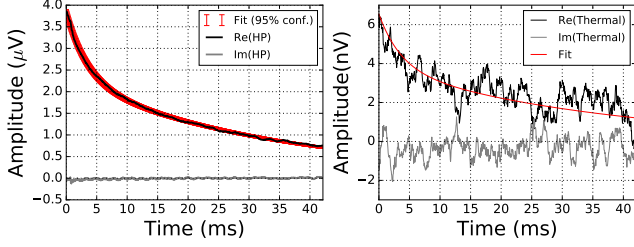
FIG. 7: Raw data from the solid echo pulse sequence is given on the left, while the data processed with a moving average is on the right.



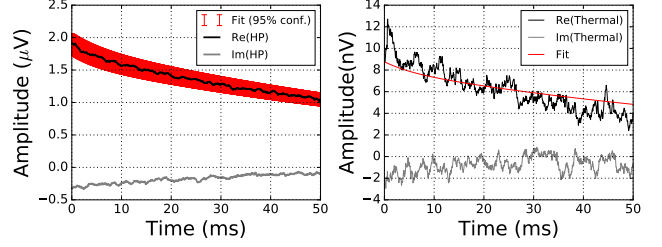
(a) D1: 1% ^{13}C . Fitted T_2 values from the biexponential model of the hyperpolarized signal were $T_{2,1} = 2.43 \pm 0.17$ ms and $T_{2,2} = 33.17 \pm 1.63$ ms. The amplitude of the thermal signal fit by scaling to the hyperpolarized signal is corrected by a factor of 1.758.



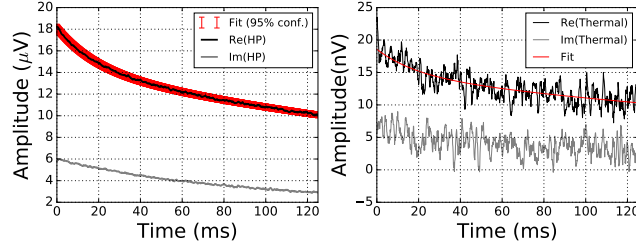
(b) D2: 10% ^{13}C . Fitted T_2 values from the biexponential model of the hyperpolarized signal were $T_{2,1} = 5.22 \pm 0.22$ ms and $T_{2,2} = 146.67 \pm 1.78$ ms. The amplitude of the thermal signal fit by scaling to the hyperpolarized signal is corrected by a factor of 1.673.



(c) D3: 25% ^{13}C . Fitted T_2 values from the biexponential model of the hyperpolarized signal were $T_{2,1} = 3.56 \pm 0.06$ ms and $T_{2,2} = 36.54 \pm 0.29$ ms. The amplitude of the thermal signal fit by scaling to the hyperpolarized signal is corrected by a factor of 1.844.



(d) D4: 50% ^{13}C . Fitted T_2 values from the biexponential model of the hyperpolarized signal were $T_{2,1} = 5.42 \pm 0.51$ ms and $T_{2,2} = 100.36 \pm 1.22$ ms. The amplitude of the thermal signal fit by scaling to the hyperpolarized signal is corrected by a factor of 1.565.



(e) D5: 100% ^{13}C . Fitted T_2 values from the biexponential model of the hyperpolarized signal were $T_{2,1} = 19.48 \pm 0.36$ ms and $T_{2,2} = 364.47 \pm 3.97$ ms. The amplitude of the thermal signal fit by scaling to the hyperpolarized signal is corrected by a factor of 1.612.

FIG. 8: T_2 measurements of all samples, showing hyperpolarized ^{13}C NMR signal on the left, thermal ^{13}C NMR signal on the right. Note the change of scale in each figure; the amplitude for each hyperpolarized signal is in μV while the amplitude for each thermal signal is in nV.

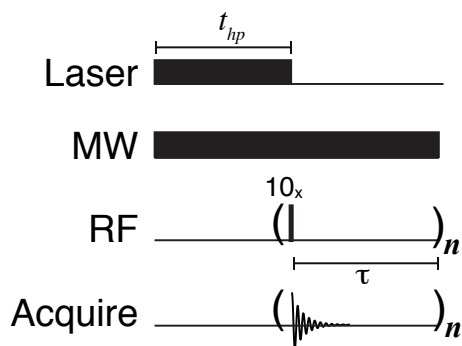
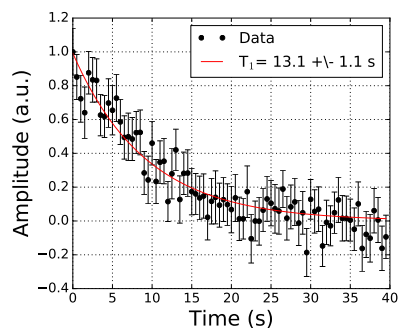
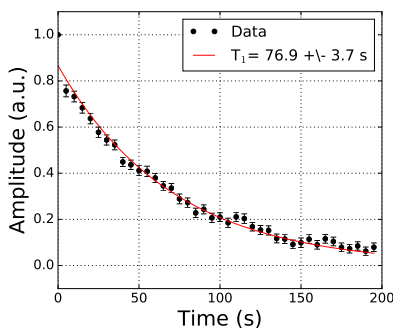


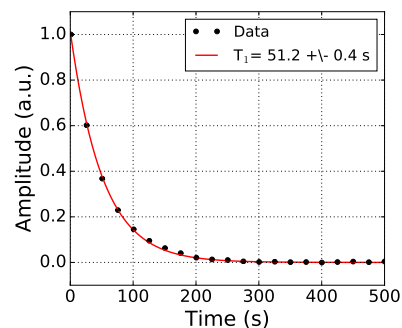
FIG. 9: Schematic of the small-flip angle T_1 measurement. The ^{13}C nuclei are hyperpolarized for a period of time t_{hp} by applying the laser and microwave excitation at the optimal saturation frequency. The laser is then switched off with an optical shutter and a series of n small-flip pulses along x are acquired spaced by a period τ . The free-induction decay is acquired after each small-flip pulse. For clarity, 10° is chosen in the schematic. The microwaves remain on during the experiment in an effort to minimize differences in NMR signal due to heating.



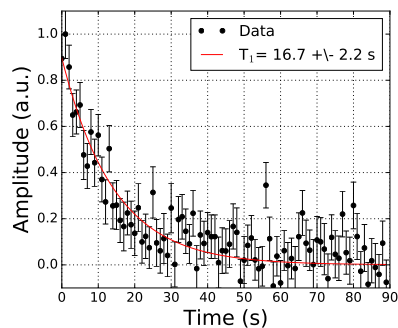
(a) D1: 1% ^{13}C . Small-flip pulse angle of 10.12° used.



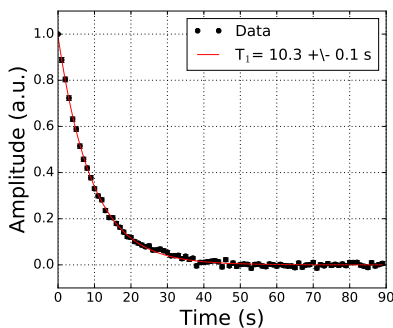
(b) D2: 10% ^{13}C . Small-flip pulse angle of 6.44° used.



(c) D3: 25% ^{13}C . T_1 data here collected point-by-point.



(d) D4: 50% ^{13}C . Small-flip pulse angle of 8.27° used.



(e) D5: 100% ^{13}C . Small-flip pulse angle of 8.27° used.

FIG. 10: $T_{1,^{13}\text{C}}$ values measured for each sample.